



OPEN

Atomic level observation of octahedral distortions at the perovskite oxide heterointerface

Ryotaro Aso¹, Daisuke Kan¹, Yuichi Shimakawa^{1,2} & Hiroki Kurata^{1,2}¹Institute for Chemical Research, Kyoto University, Uji, Kyoto 611-0011, Japan, ²Japan Science and Technology Agency, CREST, Uji, Kyoto 611-0011, Japan.SUBJECT AREAS:
STRUCTURAL PROPERTIES
TRANSMISSION ELECTRON
MICROSCOPY
CERAMICS
CHARACTERIZATION AND
ANALYTICAL
TECHNIQUESReceived
17 April 2013Accepted
1 July 2013Published
16 July 2013Correspondence and
requests for materials
should be addressed to
H.K. (kurata@eels.
kuicr.kyoto-u.ac.jp)

For perovskite oxides, ABO_3 , slight octahedral distortions have close links to functional properties. While perovskite oxide heterostructures offer a good platform for controlling functionalities, atomistic understanding of octahedral distortion at the interface has been a challenge as it requires precise measurements of the oxygen atomic positions. Here we demonstrate an approach to clarify distortions at an atomic level using annular bright-field imaging in aberration-corrected scanning transmission electron microscopy, which provides precise mappings of cation and oxygen atomic positions from distortion-minimized images. This technique revealed significant distortions of RuO_6 and ScO_6 octahedra at the heterointerface between a $SrRuO_3$ film and a $GdScO_3$ substrate. We also found that structural mismatch was relieved within only four unit cells near the interface by shifting the oxygen atomic positions to accommodate octahedral tilt angle mismatch. The present results underscore the critical role of the oxygen atom in the octahedral connectivity at the perovskite oxide heterointerface.

Many functional properties observed in perovskite oxides, ABO_3 , exhibit close couplings to slight structural distortions in the perovskite lattice, that consists of a three-dimensional network of corner-sharing BO_6 octahedra. The distortions can typically be categorized into three types: (i) cation displacements within octahedra, (ii) deformations (changes in size), and (iii) cooperative tilting (rotations) of the octahedra^{1–9}. Identification of such distortions and elucidation of their influence on properties have been important topics of investigation in fundamental materials science research as well as for applications of oxide materials in electronic devices.

It has been demonstrated that a heterostructure consisting of different ABO_3 can be used as a platform to control and tailor functionalities^{10–20}, as it can modify the degree of the coupling between lattices, electrons, and spins in the oxides. Heteroepitaxial thin films are formed by coherently growing oxides in such a way that the in-plane lattice parameters of the film are identical to those of the substrate. This introduces additional structural distortions as a result of the accommodation of elastic strain energy due to structural mismatch at the heterointerface. It has thus been widely believed that mismatch-induced strain is a primary cause for new properties emerging in the heterostructures. However, an atomic-scale understanding of how structural distortions are introduced to accommodate strain at the heterointerface is still missing and remains experimentally unaddressed because this requires precise measurements of the positions of both cations and oxygen.

The recent development of annular bright-field (ABF) imaging in aberration-corrected scanning transmission electron microscopy (STEM) allows simultaneous imaging of both light and heavy elements^{21–23}. ABF imaging combined with high angle annular dark-field (HAADF) imaging in which the contrast strongly depends on atomic number (Z)^{24,25} would be appropriate to visualize both cation and oxygen atomic positions in the oxide heterostructures. The images acquired with STEM, however, were difficult to use for precise structural analysis because of image distortions due to drifts of both the specimen and incident probe. In order to overcome this problem and obtain structural images with minimized image distortion, we used the fast multiple-image acquisition and drift correction techniques using cross correlation of the image²⁶. In addition, we were able to precisely determine the atomic positions using Bragg filtering and cubic interpolation techniques^{27,28}.

Here, we focus on a $SrRuO_3$ (SRO) epitaxial thin film grown on a $GdScO_3$ (GSO) substrate. As shown in Fig. 1, bulk SRO and GSO with a $Pbmn$ orthorhombic structure ($\sqrt{2}a_{pc} \times \sqrt{2}a_{pc} \times 2a_{pc}$) show in-phase octahedral rotation around the $[001]_{ortho}$ axis and out-of-phase rotation around the $[1-10]_{ortho}$ axis, which are described as $a^- a^- c^+$ in the Glazer notation²⁹. This indicates that the images projected along the $[001]_{ortho}$ direction are suitable

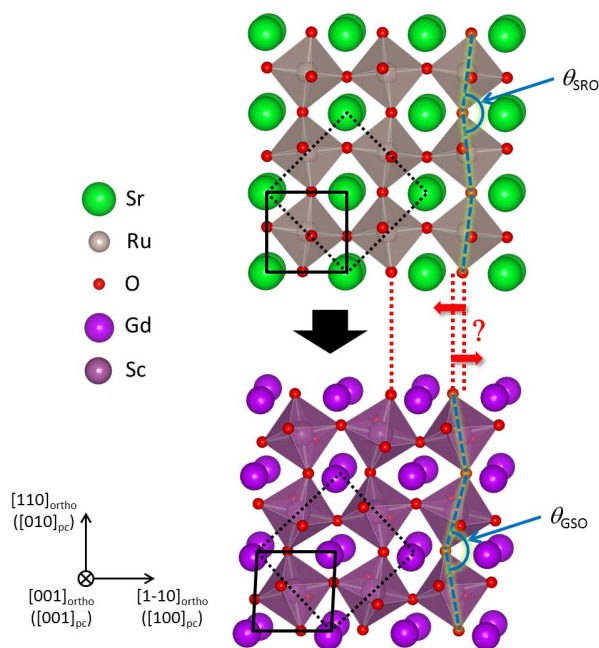


Figure 1 | Crystal structures of SrRuO₃ (SRO) and GdScO₃ (GSO). Both SRO (top) and GSO (bottom) in bulk have a *Pbmn* orthorhombic perovskite structure with $\sqrt{2}a_{pc} \times \sqrt{2}a_{pc} \times 2a_{pc}$ unit cell dimensions, where a_{pc} denotes the pseudocubic perovskite lattice parameter. In this structure, oxygen octahedra rotate in the pattern described as $a^- a^- c^+$ in the Glazer notation, where the rotations are in-phase around the $[001]_{ortho}$ axis and out-of-phase around the $[1-10]_{ortho}$ axis. This indicates that the observation along the $[001]_{ortho}$ direction allows for investigations of octahedral distortions in the SRO/GSO heterostructure. The black dotted and solid squares represent the unit cell for the orthorhombic and pseudocubic structures, respectively. The definition of the oxygen octahedral tilt angle θ (below 180° , blue dashed lines) is also included. When the SRO film is epitaxially grown on the GSO substrate (black arrow), some shifts of the oxygen atoms at the interface is expected (red arrows) due to the lattice and octahedral tilt angle mismatch between SRO and GSO.

for investigations of octahedral distortions in the SRO/GSO heterostructure. Because of the large difference in the oxygen octahedral tilt angle θ ($\theta_{SRO} = 168^\circ$, $\theta_{GSO} = 156^\circ$) as well as the lattice parameters (SRO; $a_{pc} = 3.92 \text{ \AA}$, GSO; $a_{pc} = 3.96 \text{ \AA}$), the oxygen atoms would have to be rearranged at the SRO/GSO heterointerface. Thus, the SRO/GSO heterostructure represents a good example to investigate how structural distortions are introduced as a result of structural mismatch of not only the lattice parameter but also the octahedral tilt angle.

In this study, we successfully determined the precise positions of both cations and oxygen atoms in the vicinity of the SRO/GSO heterointerface from HAADF- and ABF-STEM images with minimized image distortion. This approach allows detection of oxygen octahedral distortions as well as cation lattice distortions due to accommodation of structural mismatch at the heterointerface. We found that the strained SRO thin film has a RuO₆ octahedral tilt, the angle of which reaches the value for the bulk except in the vicinity of the interface despite the film being under tensile strain. We also revealed that the mismatch of the octahedral tilt angles is accommodated by displacing only the oxygen atoms within only four unit cells across the heterointerface.

Results

A 15 nm-thick SRO thin film was grown on a (110) GSO substrate by pulsed laser deposition, as described in a previous paper³⁰. We

confirmed, by X-ray reciprocal space mapping, that the fabricated (110) SRO film has a distorted orthorhombic structure with no crystallographic twins³¹. Figure 2a shows the HAADF image of the heterostructure of the SRO film and GSO substrate taken along the $[001]_{ortho}$ direction. The HAADF image which produces contrast depending on the atomic number (Z) indicates the constituent atomic positions as bright spots. The insets are simulated HAADF images for the bulk SRO and GSO, which are in good accord with the contrast of the observed image. In the GSO substrate area, the image contrast of the Gd atomic columns is slightly distorted, reflecting the projection of displaced Gd atoms (see Fig. 1). This indicates that a slight atomic shift can be detected precisely from the HAADF image. The image also shows that there are no misfit dislocations in the heterostructure, consistent with our previous X-ray structural characterizations³⁰. Figure 2b shows intensity profiles of the HAADF image across the heterointerface. The intensity profile of A-site cations (along the red line in Fig. 2a) gives atomic positions of Sr ($Z = 38$) in the film (green in Fig. 2b) and Gd ($Z = 64$) in the substrate (purple in Fig. 2b). On the other hand, the intensity profile of B-site cations (along the blue line in Fig. 2a) gives atomic positions of Ru ($Z = 44$) in the film (gray in Fig. 2b) and Sc ($Z = 21$) in the substrate (pink in Fig. 2b). From the point where the HAADF intensities change significantly, we can identify the interface of the heterostructure. Termination of the GSO substrate is identified to be a ScO₂ layer^{32,33} and the SRO epitaxial thin film begins from the SrO layer. Figure 2c shows the ABF image taken from the same region as the HAADF image (Fig. 2a), where the atomic positions are visualized as dark contrast. We can clearly see oxygen columns in the image, which was verified from the inserted simulation images. This image allows determination of the shapes of corner-shared oxygen octahedra projected along the $[001]_{ortho}$ direction as denoted by the red solid open squares. We are thus successful in investigating the connectivity of the tilted octahedra across the interface between the SRO thin film and GSO substrate.

To quantitatively analyze lattice distortions induced by the structural mismatch, we measured the positions of A-site cations from the HAADF image at sub-pixel resolution using the “Find Peaks” option incorporated in the Peak Pairs Analysis software^{27,28}. Figure 3a shows the variation of the cation lattice spacing extracted from the HAADF image (Fig. 2a) of which a portion is shown on the left. The interatomic distances along the out-of-plane (red solid squares) and in-plane (blue solid circles) directions were determined by averaging over 18 unit cells of the pseudocubic perovskite lattice along the $[1-10]_{ortho}$ direction (the in-plane direction). The measured in-plane lattice parameters in the SRO film ($3.957 \pm 0.050 \text{ \AA}$) are nearly equal to that of the GSO substrate (3.96 \AA , purple dotted line), which is consistent with the fact that the film was coherently grown on the substrate with 1.0% tensile strain. On the other hand, the measured out-of-plane lattice parameters in the SRO film ($3.915 \pm 0.039 \text{ \AA}$) have almost the same value as that of the bulk SRO (3.92 \AA , green dotted line). These results indicate that the pseudocubic unit cell of the SRO film is distorted by the epitaxial strain and elongates only along the in-plane direction. Interestingly, the out-of-plane lattice parameters drastically change across the interface. We note that the ScO₂ layer at the interface (orange dotted line) is heavily distorted with the out-of-plane lattice parameter identical to that of the film region. This suggests that the distorted ScO₂ layer plays an important role in the mismatch accommodation at the interface.

Figure 3b shows the variation of the oxygen octahedral tilt angles θ , which were extracted from the oxygen atomic positions in the ABF image (Fig. 2c). The projected ScO₆ (purple boxes) and RuO₆ (green boxes) octahedra are also drawn in Fig. 3b. The tilt angles were determined by averaging alternately over 18 unit cells of pseudocubic perovskite lattice along the $[1-10]_{ortho}$ direction (the in-plane direction) because of the characteristic orthorhombic lattice. We see that except in the vicinity of the interface (yellow region), each

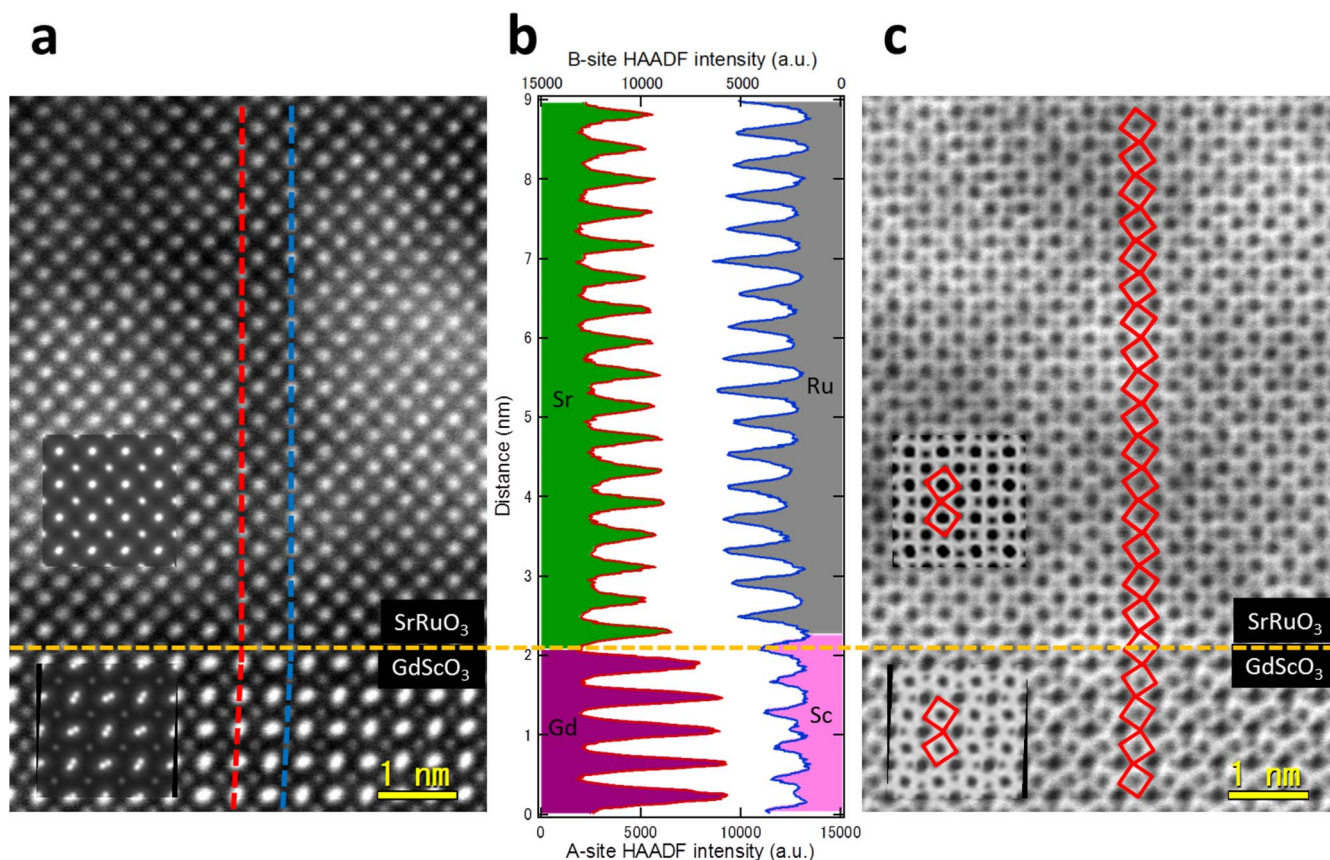


Figure 2 | Atomic-scale structural characterization of SRO/GSO heterostructure by high-resolution HAADF- and ABF-STEM techniques. (a), High-resolution HAADF image of the heterostructure of the SRO thin film and GSO substrate taken along the $[001]_{\text{ortho}}$ direction. Simulated HAADF images of bulk SRO and GSO with the orthorhombic structure are also inserted in the image. (b), HAADF intensity profiles of A-site (left side) and B-site (right side) cations across the interface. The data were collected along the $[110]_{\text{ortho}}$ direction (the out-of-plane direction) as indicated by red and blue dashed lines for A- and B-site cationic rows in Fig. 2a, respectively. In the profiles, the intensities colored green, purple, gray, and pink represent the HAADF intensities of Sr ($Z = 38$), Gd ($Z = 64$), Ru ($Z = 44$), and Sc ($Z = 21$) atomic columns, respectively. Then, we can define the position of the heterointerface to the topmost ScO_2 layer of the substrate as denoted with the orange dashed line. (c), ABF image taken from the same region as the HAADF image (Fig. 2a). In the ABF image, the oxygen atoms are clearly visible, revealing the projected shape of each oxygen octahedron and the connectivity of the octahedra across the heterointerface as indicated with the red open squares.

octahedral tilt angle in the SRO film and GSO substrate is nearly constant in the value of each bulk counterpart. Thus, the mismatch in the oxygen octahedral tilt angle is adjusted only near the SRO/GSO heterointerface, indicating that the rotation pattern of the substrate penetrates poorly into the epitaxial thin film.

The above results lead us to further investigations of the octahedral connectivity at the interface in the perovskite oxide heterostructure. The perovskite oxide epitaxial thin films often accommodate the additional octahedral rotations or tilts due to the octahedral connection between the film and substrate^{1–5,30,34–44}. Hence, the oxygen octahedra across the heterointerface are expected to be deformed drastically. Figure 4a shows the variation of the oxygen octahedral tilt angles θ across the SRO/GSO interface. Within only four unit cells around the interface, the tilt angle θ changes from 156° for the GSO substrate to 168° for the SRO film, and the tilt angles for the film in the vicinity of the heterointerface (yellow region) are slightly smaller than those of the SRO film away from the interface. Given that the oxygen octahedra in the perovskite structure are connected by sharing the oxygen atom in its corner, the drastic changes in the octahedral tilt angle observed at the interface can be ascribed to modifications of the oxygen atom positions. We plotted the displacements of apical oxygen atoms of the octahedra along the in-plane direction, Δx , across the heterointerface in Fig. 4c. The variation of Δx shows a similar trend to that of the tilt angles (Fig. 4a). The large

displacement of 43 pm of the apical oxygen atoms in the GSO substrate is adjusted to the displacements (~ 21 pm) for the SRO thin film within only four unit cells around the heterointerface. Note also that the bottom apical oxygen atoms in the topmost ScO_6 octahedra at the interface are also displaced about 5 pm. The octahedral tilt angle between the topmost and second ScO_6 octahedral layers in the GSO substrate (indicated by the red dashed circle in Fig. 4a) thus slightly increases from that of the bulk GSO. These results indicate the significant distortion of the topmost ScO_6 octahedra of the substrate, which correlates with the lattice distortion of the ScO_2 layer at the heterointerface as mentioned above (see Fig. 3a).

Discussion

Based on our observations of the cation lattice and the oxygen octahedra, we constructed an atomic structure model of the heterointerface between the SRO film and GSO substrate (Fig. 4b). Accommodation of the octahedral tilt angle mismatch between the SRO and GSO results in significant distortion of the topmost ScO_6 octahedral layer of the substrate as well as the in-plane displacement of the apical oxygen atoms near the heterointerface. It is worth pointing out that the in-plane cation lattice mismatch in the SRO thin film is still accommodated in the entire film region. This suggests that the mechanisms for accommodation of the cation lattice mismatch and the octahedral tilt angle mismatch are different. The cation

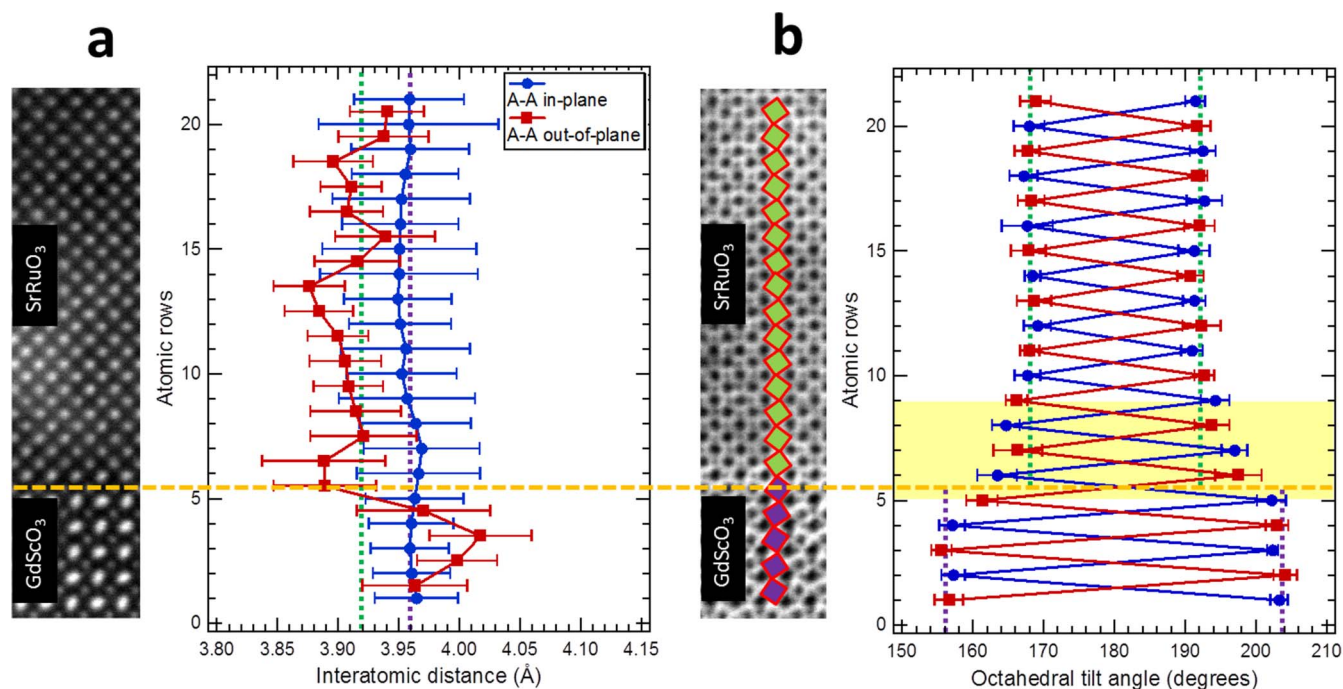


Figure 3 | Quantitative analysis of octahedral distortions across SRO/GSO heterointerface. (a), Variation of the out-of-plane (red) and in-plane (blue) lattice spacing extracted from the HAADF image in Fig. 2a. For clarity, a portion of the HAADF image is also shown on the left next to the graph. Each spacing was determined from the average over 18 unit cells of the pseudocubic perovskite lattice layer along the $[1-10]_{\text{ortho}}$ direction (the in-plane direction). The error bars show standard deviation with respect to averaging for each lattice layer. The pseudocubic lattice parameters of the SRO ($a_{\text{pc}} = 3.92 \text{ \AA}$) and GSO ($a_{\text{pc}} = 3.96 \text{ \AA}$) in bulk are indicated by the dotted lines in green and purple, respectively. (b), Variation of the oxygen octahedral tilt angle extracted from the ABF image in Fig. 2c. For clarity, a portion of the ABF image is also shown on the left next to the graph. The squares drawn in the ABF image represent the projected shapes of the ScO₆ (purple) and RuO₆ (green) octahedra. The tilt angle θ along the $[110]_{\text{ortho}}$ direction was determined by averaging alternately over 18 unit cells of the pseudocubic perovskite lattice layer along the $[1-10]_{\text{ortho}}$ direction (the in-plane direction). The error bars show standard deviation with respect to averaging alternately for each lattice layer. In the graph, the dotted lines in green and purple indicate the octahedral tilt angles of SRO and GSO in bulk, respectively. In the interface region (yellow box), the mismatch in the octahedral tilt angle between SRO and GSO is accommodated.

lattice mismatch can be easily accommodated by a slight shift of the cations, and as a result, the thin films maintain the framework of the perovskite structure under the lattice mismatch-induced strain. On the other hand, the octahedral tilt is predominantly caused by the size mismatch of the constituent A- and B-site cations according to the Goldschmidt tolerance factor^{4,8,9,45}. Thus, the oxygen octahedral tilt angles are constant in the film and the substrate, and their difference should be accommodated only near the heterointerface at which the size balance of the A- and B-site cations changes. Such mismatch accommodation in the oxygen tilt angle is achieved mainly by in-plane displacements of the apical oxygen atoms of the octahedra. This explains our observations and demonstrates that the oxygen atomic positions in the perovskite framework play a dominant role in the accommodation of the octahedral tilt angle mismatch.

In summary, from complementary HAADF- and ABF-STEM images with minimized image distortions, we were able to reveal octahedral distortions resulting from accommodation of structural mismatch at the interface between the SRO film and GSO substrate. The octahedral tilt angle in the strained SRO thin film is comparable to that in the bulk SRO, and mismatch of the octahedral tilt angle between the film and substrate is accommodated within only four unit cells around the heterointerface. This accommodation results in significant distortions of the topmost ScO₆ octahedral layer of the substrate as well as in-plane displacement of the apical oxygen atoms near the interface. These results highlight the fact that the oxygen arrangement around the heterointerface plays a critical role in the epitaxial strain accommodation in the perovskite oxide heterostructures.

Methods

Sample preparation. A 15 nm-thick SrRuO₃ (SRO) epitaxial thin film was grown on a $(110)_{\text{ortho}}$ GdScO₃ (GSO) substrate by pulsed laser deposition (the subscript *ortho* denotes the orthorhombic structure). The lattice constants of the GSO substrate are $a_{\text{ortho}} = 5.45 \text{ \AA}$, $b_{\text{ortho}} = 5.75 \text{ \AA}$, and $c_{\text{ortho}} = 7.93 \text{ \AA}$. Thus the averaged lattice mismatch between SRO ($a_{\text{ortho}} = 5.57 \text{ \AA}$, $b_{\text{ortho}} = 5.53 \text{ \AA}$, and $c_{\text{ortho}} = 7.85 \text{ \AA}$ in bulk) and the substrate, $(a_{\text{sub}} - a_{\text{SRO}})/a_{\text{SRO}}$, where a_{sub} and a_{SRO} are the pseudocubic lattice parameters of the GSO substrate and the SRO film, is $+1.0\%$ (tensile strain). Details of the thin film fabrication process are given in our previous report³⁰. Briefly, the substrate temperature and partial oxygen pressure during the deposition of the SRO layer were kept at 700 °C and 100 mTorr, respectively. The film thickness was determined from the period of the Laue oscillation observed in the X-ray 2θ - θ diffraction pattern. We confirmed that the fabricated SRO thin film has a slightly distorted orthorhombic structure and that there are no crystallographic twins³¹.

Microscopy. For cross-sectional TEM observations, the thin film specimen was thinned down to electron transparency by mechanical polishing and Ar-ion milling⁴⁶. STEM images were acquired at room temperature in a spherical aberration corrected STEM (JEM-9980TKP1; accelerating voltage = 200 kV, $C_s = -0.025 \text{ mm}$, $C_5 = 15 \text{ mm}$) equipped with a cold field emission gun. The annular detection angle for HAADF was 50–133 mrad and that for ABF was 11–23 mrad because the convergent semi-angle of the incident probe was 23 mrad. 50 HAADF and 50 ABF images were acquired from the same area with a short dwell time (ca. 4.2 $\mu\text{s}/\text{pixel}$). Then, the multiple images were superimposed after correcting for the relative drifts²⁶. This procedure provides high resolution STEM images with improved signal-to-noise (SN) ratio and with minimized image distortion. Measurements of the atomic positions were carried out in the STEM images at sub-pixel resolution using Bragg filtering and cubic interpolation techniques in the “Find Peaks” option (Peak Pairs Analysis software package by HREM Research)^{27,28}.

Simulations. For reliable interpretation of the HAADF and ABF image contrasts, STEM image simulation was performed using multislice simulation software (WinHREM by HREM Research). The simulated images were obtained using an aberration-corrected probe with $C_s = -0.025 \text{ mm}$, $C_5 = 15 \text{ mm}$ and convergent

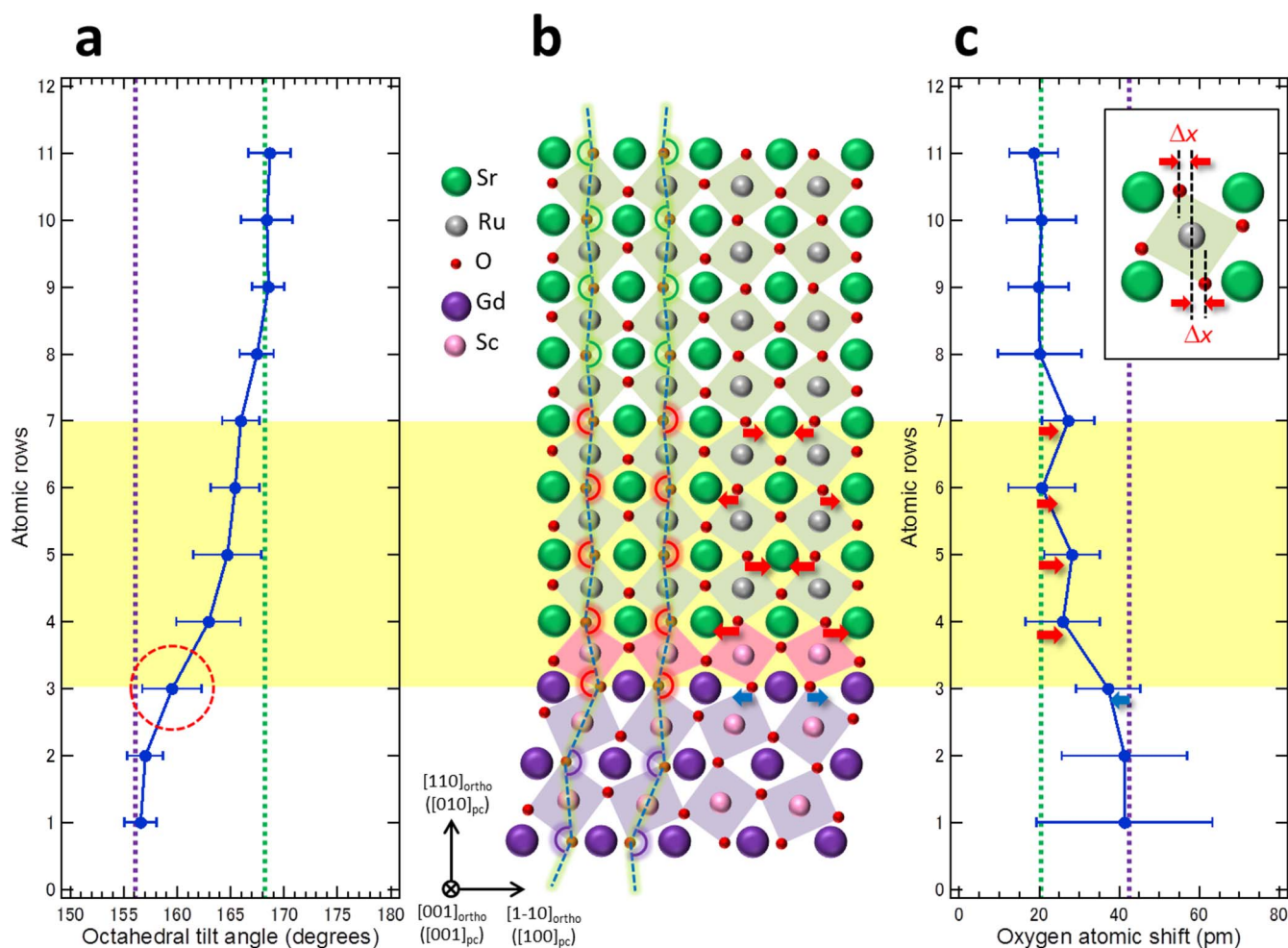


Figure 4 | Atomic-scale view of the octahedral distortions due to the structural mismatch accommodation at SRO/GSO heterointerface. (a), Oxygen octahedral tilt variation extracted from the ABF image in Fig. 2c, where the tilt angles were averaged as an angle below 180° over 18 pseudocubic unit cells along the $[1-10]_{\text{ortho}}$ direction (the in-plane direction). The graph shows the octahedral tilt angles θ of the bulk SRO (green dotted line) and GSO (purple dotted line). The error bars show standard deviation with respect to averaging for each lattice layer. In the graph, the red dashed circle indicates the octahedral tilt angle between the topmost and second ScO_6 octahedral layers in the GSO substrate. (b), Structural model around the heterointerface between the SRO thin film and GSO substrate projected along the $[001]_{\text{ortho}}$ direction. The termination layer of the GSO substrate is a ScO_2 layer and the first layer of the SRO epitaxial thin film is a SrO layer, where ScO_6 octahedra (pink squares) at the heterointerface share oxygen atoms in the SrO layers. Blue dashed lines represent the oxygen octahedral tilt angles in Fig. 4a. (c), Oxygen atomic shift variation extracted from the ABF image in Fig. 2c, where the oxygen atomic shift Δx is defined as the distance from the middle position between A-site cations along the in-plane direction (as inserted in Fig. 4c). The graph shows the oxygen atomic shifts in the bulk SRO (green dotted line) and GSO (purple dotted line). Red and blue arrows represent the oxygen atomic shifts from that of the bulk SRO and GSO, respectively, the directions of which are shown in Fig. 4b. The yellow box in the vicinity of the heterointerface represents the region where the tilt angle mismatch is accommodated.

semi-angle of 23 mrad. The annular detection angle for HAADF in the simulations was 50–133 mrad, and that for ABF was 11–23 mrad.

- Rondinelli, J. M., May, S. J. & Freeland, J. W. Control of octahedral connectivity in perovskite oxide heterostructures: An emerging route to multifunctional materials discovery. *MRS Bulletin* **37**, 261–270 (2012).
- Rondinelli, J. M. & Spaldin, N. A. Structure and properties of functional oxide thin films: Insights from electronic-structure calculations. *Adv. Mater.* **23**, 3363–3381 (2011).
- Zayak, A. T., Huang, X., Neaton, J. B. & Rabe, K. M. Structural, electronic, and magnetic properties of SrRuO_3 under epitaxial strain. *Phys. Rev. B* **74**, 094104 (2006).
- Vailionis, A. *et al.* Misfit strain accommodation in epitaxial ABO_3 perovskites: Lattice rotations and lattice modulations. *Phys. Rev. B* **83**, 064101 (2011).
- He, J., Borisevich, A., Kalinin, S. V., Pennycook, S. J. & Pantelides, S. T. Control of octahedral tilts and magnetic properties of perovskite oxide heterostructures by substrate symmetry. *Phys. Rev. Lett.* **105**, 227203 (2010).
- Gopalan, V. & Litvin, D. B. Rotation-reversal symmetries in crystals and handed structures. *Nat. Mater.* **10**, 376–381 (2011).
- Garcia-Fernandez, P., Aramburu, J. A., Barriuso, M. T. & Moreno, M. Key role of covalent bonding in octahedral tilting in perovskites. *J. Phys. Chem. Lett.* **1**, 647–651 (2010).
- Woodward, P. M. Octahedral tilting in perovskites. I. Geometrical considerations. *Acta Cryst. B* **53**, 32–43 (1997).
- Woodward, P. M. Octahedral tilting in perovskites. II. Structure stabilizing forces. *Acta Cryst. B* **53**, 44–66 (1997).
- Hwang, H. Y. *et al.* Emergent phenomena at oxide interfaces. *Nat. Mater.* **11**, 103–113 (2012).
- Ohtomo, A. & Hwang, H. Y. A high-mobility electron gas at the $\text{LaTiO}_3/\text{SrTiO}_3$ heterointerface. *Nature* **427**, 423–426 (2004).
- Lee, J. H. *et al.* A strong ferroelectric ferromagnet created by means of spin-lattice coupling. *Nature* **466**, 954–958 (2010).
- Zeches, R. J. *et al.* A strain-driven morphotropic phase boundary in BiFeO_3 . *Science* **326**, 977–980 (2009).
- Choi, K. J. *et al.* Enhancement of ferroelectricity in strained BaTiO_3 thin films. *Science* **306**, 1005–1009 (2004).
- Lee, H. N., Christen, H. M., Chisholm, M. F., Rouleau, C. M. & Lowndes, D. H. Strong polarization enhancement in asymmetric three-component ferroelectric superlattices. *Nature* **433**, 395–399 (2005).



16. Bousquet, E. *et al.* Improper ferroelectricity in perovskite oxide artificial superlattices. *Nature* **452**, 732–736 (2008).
17. Boris, A. V. *et al.* Dimensionality control of electronic phase transitions in nickel-oxide superlattices. *Science* **332**, 937–940 (2011).
18. Wakabayashi, Y. Near-surface structural study of transition metal oxides to understand their electronic properties. *J. Phys.: Condens. Matter* **23**, 483001 (2011).
19. Segal, Y. *et al.* Dynamic evanescent phonon coupling across the $\text{La}_{1-x}\text{Sr}_x\text{MnO}_3/\text{SrTiO}_3$ interface. *Phys. Rev. Lett.* **107**, 105501 (2011).
20. Schlom, D. G. *et al.* Strain tuning of ferroelectric thin films. *Annu. Rev. Mater. Res.* **37**, 589–626 (2007).
21. Findlay, S. D. *et al.* Robust atomic resolution imaging of light elements using scanning transmission electron microscopy. *Appl. Phys. Lett.* **95**, 191913 (2009).
22. Findlay, S. D. *et al.* Dynamics of annular bright field imaging in scanning transmission electron microscopy. *Ultramicroscopy* **110**, 903–923 (2010).
23. Haruta, M. & Kurata, H. Direct observation of crystal defects in an organic molecular crystals of copper hexachlorophthalocyanine by STEM-EELS. *Sci. Rep.* **2**, 252 (2012).
24. Pennycook, S. J. & Jesson, D. E. High-resolution Z-contrast imaging of crystals. *Ultramicroscopy* **37**, 14–38 (1991).
25. Pennycook, S. J. & Jesson, D. E. High-resolution incoherent imaging of crystals. *Phys. Rev. Lett.* **64**, 938–941 (1990).
26. Saito, M. *et al.* Local crystal structure analysis with 10-pm accuracy using scanning transmission electron microscopy. *J. Electron Microsc.* **58**(3), 131–136 (2009).
27. Galindo, P. L. *et al.* The Peak Pair algorithm for strain mapping from HRTEM images. *Ultramicroscopy* **107**, 1186–1193 (2007).
28. Galindo, P., Pizarro, J., Molina, S. & Ishizuka, K. High resolution peak measurement and strain mapping using Peak Pair analysis. *Microsc. Anal.* **23**(2), 23–25 (2009).
29. Glazer, A. M. The classification of tilted octahedra in perovskites. *Acta Cryst. B* **28**, 3384–3392 (1972).
30. Kan, D., Aso, R., Kurata, H. & Shimakawa, Y. Thickness-dependent structure-property relationships in strained (110) SrRuO_3 thin films. *Adv. Funct. Mater.* **23**, 1129–1136 (2013).
31. Kan, D. & Shimakawa, Y. Geometric-shape-dependent structural transition behavior in (110) SrRuO_3 epitaxial thin films. *J. Appl. Phys.* **111**, 093532 (2012).
32. Kleibecker, J. E. *et al.* Structure of singly terminated polar DyScO_3 (110) surfaces. *Phys. Rev. B* **85**, 165413 (2012).
33. Kleibecker, J. E. *et al.* Atomically defined rare-earth scandate crystal surfaces. *Adv. Funct. Mater.* **20**, 3490–3496 (2010).
34. Borisevich, A. Y. *et al.* Suppression of octahedral tilts and associated changes in electronic properties at epitaxial oxide heterostructure interfaces. *Phys. Rev. Lett.* **105**, 087204 (2010).
35. Jia, C. L. *et al.* Oxygen octahedron reconstruction in the $\text{SrTiO}_3/\text{LaAlO}_3$ heterointerfaces investigated using aberration-corrected ultrahigh-resolution transmission electron microscopy. *Phys. Rev. B* **79**, 081405(R) (2009).
36. Borisevich, A. Y. *et al.* Mapping octahedral tilts and polarization across a domain wall in BiFeO_3 from Z-contrast scanning transmission electron microscopy image atomic column shape analysis. *ACS Nano* **4**, 6071–6079 (2010).
37. Kan, D. & Shimakawa, Y. Strain effect on structural transition in SrRuO_3 epitaxial thin films. *Cryst. Growth Des.* **11**, 5483–5487 (2011).
38. Rondinelli, J. M. & Spaldin, N. A. Substrate coherency driven octahedral rotations in perovskite oxide films. *Phys. Rev. B* **82**, 113402 (2010).
39. Chang, S. H. *et al.* Thickness-dependent structural phase transition of strained SrRuO_3 ultrathin films: The role of octahedral tilt. *Phys. Rev. B* **84**, 104101 (2011).
40. May, S. J. *et al.* Control of octahedral rotations in $(\text{LaNiO}_3)_n/(\text{SrMnO}_3)_m$ superlattices. *Phys. Rev. B* **83**, 153411 (2011).
41. Zayak, A. T., Huang, X., Neaton, J. B. & Rabe, K. M. Manipulating magnetic properties of SrRuO_3 and CaRuO_3 with epitaxial and uniaxial strains. *Phys. Rev. B* **77**, 214410 (2008).
42. Hatt, A. J. & Spaldin, N. A. Structural phases of strained LaAlO_3 driven by octahedral tilt instabilities. *Phys. Rev. B* **82**, 195402 (2010).
43. May, S. J. *et al.* Quantifying octahedral rotations in strained perovskite oxide films. *Phys. Rev. B* **82**, 014110 (2010).
44. Rondinelli, J. M. & Coh, S. Large isosymmetric reorientation of oxygen octahedra rotation axes in epitaxially strained perovskites. *Phys. Rev. Lett.* **106**, 235502 (2011).
45. Goodenough, J. B. Electronic and ionic transport properties and other physical aspects of perovskites. *Rep. Prog. Phys.* **67**, 1915–1993 (2004).
46. Dieterle, L., Butz, B. & Müller, E. Optimized Ar^+ -ion milling procedure for TEM cross-section sample preparation. *Ultramicroscopy* **111**, 1636–1644 (2011).

Acknowledgements

This work was partially supported by a Grant-in-Aid for Scientific Research (Grant No. 24760009), and a grant for the Joint Project of Chemical Synthesis Core Research Institutions from the Ministry of Education, Culture, Sports, Science and Technology of Japan. The work was also supported by the Japan Science and Technology Agency, CREST.

Author contributions

R.A. and D.K. conceived the idea and initiated the project. D.K. and Y.S. fabricated the samples. R.A. and H.K. collected and analyzed the STEM data. Y.S. and H.K. supervised the project. All authors discussed the experimental data and co-wrote the manuscript.

Additional information

Competing financial interests: The authors declare no competing financial interests.

How to cite this article: Aso, R., Kan, D., Shimakawa, Y. & Kurata, H. Atomic level observation of octahedral distortions at the perovskite oxide heterointerface. *Sci. Rep.* **3**, 2214; DOI:10.1038/srep02214 (2013).



This work is licensed under a Creative Commons Attribution-NonCommercial-NoDerivs 3.0 Unported license. To view a copy of this license, visit <http://creativecommons.org/licenses/by-nc-nd/3.0>